

Phononic crystal Luneburg lens for omnidirectional elastic wave focusing and energy harvesting

S. Tol, F. L. Degertekin, and A. Erturk^{a)}

G. W. Woodruff School of Mechanical Engineering, Georgia Institute of Technology, Atlanta, Georgia 30332, USA

(Received 1 May 2017; accepted 22 June 2017; published online 6 July 2017)

We explore a phononic crystal Luneburg lens through design, fabrication, and analysis for omnidirectional elastic wave focusing and enhanced energy harvesting both numerically and experimentally. The proposed lens is formed using hexagonal unit cells with blind holes of different diameters, which are determined according to the Luneburg lens refractive index distribution obtained by finite-element simulations of the lowest asymmetric mode Lamb wave band structure. Wave simulations are performed numerically under plane wave excitation from a line source, and focusing is observed at the opposite border of the lens with respect to the incident wave direction. Numerically simulated elastic wave focusing results are validated through a set of experiments. Omnidirectionality is demonstrated by testing the lens under plane wave excitation for different angles of incidence. With piezoelectric energy harvesters located at the boundary of the phononic crystal Luneburg lens, more than an order of magnitude larger power output can be extracted as compared to the baseline case of energy harvesting without the lens under the same plane wave excitation. *Published by AIP Publishing.* [<http://dx.doi.org/10.1063/1.4991684>]

Elastic wave propagation in artificially structured phononic crystals (PCs) has recently received growing attention.^{1,2} PCs usually employ a periodic architecture with a spatial modulation of elastic and mass properties on a scale comparable to the wavelength of elastic/acoustic waves. Due to their unique characteristics such as bandgaps^{1–4} and the ability to reduce the phase and group velocities,⁵ PCs offer the potential for a variety of applications including sound attenuation,^{6,7} wave filtering,⁸ subwavelength imaging,^{9,10} refractive acoustic devices such as Gradient-Index (GRIN) PC lens designs,^{11–13} among others. In addition to these applications, concepts from phononic crystals and acoustic metamaterials^{1,2} may yield unprecedented approaches for enhanced energy harvesting. Relatively few research efforts have explored this area for energy harvesting with a focus on phononic crystal bandgaps,^{14,15} locally resonant metamaterials,¹⁶ acoustic black hole¹⁷ and cavity^{18–20} concepts, defects and imperfections,^{21–23} funnels,²³ elliptical and parabolic mirrors,^{23–25} and GRIN-PC lens concepts.²⁶ While the GRIN-PC lens we explored recently²⁶ is a very effective design implemented to focus propagating flexural waves (A_0 mode Lamb wave) for enhanced piezoelectric energy harvesting, its performance is susceptible to the orientation of the incident plane wave. Hence, in this paper, our aim is to alleviate the directivity issue by means of a PC Luneburg lens owing to its omnidirectional focusing characteristics. Outside the domain of energy harvesting literature, Climente *et al.*²⁷ designed a Luneburg lens for flexural waves by locally varying the plate thickness in the circular lens region and numerically showed omnidirectional wave focusing. In the present work, we extend the Luneburg lens concept to a practical PC design with blind hole-based unit cells, provide

experimental validations for omnidirectional focusing, and explore energy harvesting performance enhancement.

In the existing literature of phononic crystals, GRIN-PC lens concepts have been demonstrated (mostly numerically) by means of material,¹¹ diameter,²⁸ and height²⁹ variations of periodically arranged stubs, or hole size variation of perforated plates,^{30,31} or local variations of plate thickness.²⁷ In this work, we present a PC Luneburg lens based on hexagonal unit cells of different blind hole diameters and demonstrate its omnidirectional focusing performance and energy harvesting implementation. The hexagonal unit cell design is convenient to approximate the circular Luneburg lens geometry, while the blind hole concept offers structural integrity (as compared to full perforation via through holes) and eliminates mass addition (as compared to using stubs). The orientation and size of the blind holes are based on the Luneburg gradient distribution which is calculated from dispersion curves of the A_0 mode Lamb wave. The refractive index profile of a Luneburg lens is defined as

$$n(r) = \sqrt{2 - \frac{r^2}{R^2}}, \quad (1)$$

where $n(r)$ is the refractive index as a function r , which is the radial position of the unit cell from the center of the lens, and R is the lens radius. The refractive index can be calculated using $n = v/v_{\Gamma M}$, where $v_{\Gamma M}$ is the phase velocity in the ΓM direction of the unit cell [Figs. 1(a) and 1(b)] and v is the reference phase velocity of the A_0 mode Lamb wave in a homogenous aluminum plate of the same thickness (which is the thickness of the uniform plate portion without the lens). We used finite element simulations (COMSOL Multiphysics[®]) to calculate the band structures of A_0 mode waves propagating along the ΓM orientation in phononic crystals for various blind hole diameters (d) with an

^{a)}Author to whom correspondence should be addressed: alper.erturk@me.gatech.edu

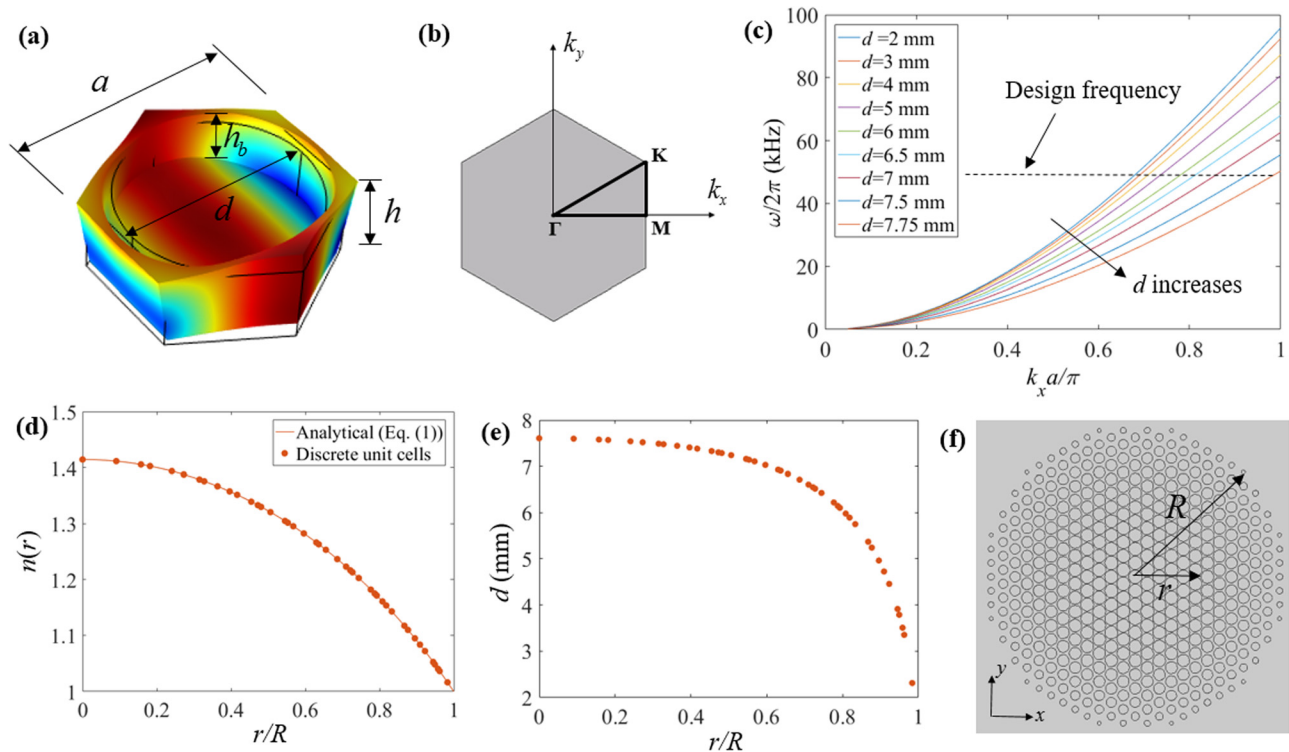


FIG. 1. (a) Hexagonal unit cell and (b) its first Brillouin zone; (c) band structure of the A_0 mode Lamb wave for various blind hole diameters over a range of frequencies including the design frequency (50 kHz); (d) Luneburg lens refractive index profile and (e) corresponding blind hole diameters versus dimensionless lens radius at the design frequency; and (f) resulting PC Luneburg lens.

aluminum plate thickness of $h = 3.175$ mm, blind hole depth of $h_b = 2.175$ mm, and unit cell size of $a = 8$ mm [as illustrated in Fig. 1(a)]. The first Brillouin zone of the hexagonal unit cell design is shown in Fig. 1(b). In the numerical simulations, Floquet periodicity was applied at the sides of the unit cell as boundary conditions. By parametric sweeping of the wave vector k_x from 0 to π/a , eigenfrequencies were computed at each wavenumber value and the band structure was obtained as shown in Fig. 1(c). Note that considering the dispersion only in the x -direction [i.e., ΓM -direction in Fig. 1(b)] provides satisfactory results in GRIN-PC lens design due to very small anisotropy of the hexagonal unit cell structure with blind holes (which is confirmed by simulations not shown here). We assumed a design frequency of 50 kHz as in our previous work^{23–26} to have practical dimensions in the experimental setup. Based on the Luneburg concept, we designed an approximate circular lens with the refractive index profile shown in Fig. 1(d) (both the analytical Eq. (1) and discrete unit cell data are shown). The blind hole diameters corresponding to the discrete refractive index profile of the unit cells are shown in Fig. 1(e). A 6-fold symmetry was employed to approximate circular symmetry and a lens of 176 mm diameter was formed by using 433 hexagonal unit cells as shown in Fig. 1(f). Note that the blind hole unit cells with the largest diameters are located around the center of the lens while the ones with the smallest diameters are located towards the edges. As a result, when a plane wave is incident upon the Luneburg lens, the wave front moves increasingly slower as it approaches the center of the lens and eventually converges at the focal spot on the lens boundary on the opposite side of the incident wave direction.

Finite element simulations were performed to validate wave focusing capability of the Luneburg lens designed using the outlined PC approach. The aluminum plate was excited by a line source which acts as a boundary load with 4 cycles of sine burst with a Gaussian pulse window at a center frequency of 50 kHz. Low reflection boundary condition was applied at the sides, which is not very critical since the simulation domain was selected as $760 \text{ mm} \times 305 \text{ mm}$ so that the critical transient signals were obtained without interference of the reflections from the boundaries. As a rule of thumb in time-dependent numerical simulations, mesh size was set to satisfy 7 mesh elements per wavelength so that the wave was equally resolved in space. Using the relationship between the mesh size and time step length (Courant-Friedrichs-Lewy number ~ 0.2), time stepping was set so that the optimal solution was obtained. Figures 2(a) and 2(b) illustrate that the wave travels faster close to the borders and slower around the center as it propagates through the lens. The root-mean-square (RMS) wave field was obtained as shown in Fig. 2(c) by integrating the measured response over time. From the instantaneous and RMS wave fields, it is clearly seen that the plane wave focuses at the opposite border.

In order to confirm omnidirectional focusing performance, the simulations were repeated for 30° angle of incidence as shown in Fig. 3. This particular angle represents incidence from a corner of the PC Luneburg lens that is approximated using hexagonal unit cells [cf. Figs. 1(b) and 1(f)]. The results summarized in Fig. 3 show that similar focusing performance is obtained for this incidence angle as well, demonstrating that the desired omnidirectional behavior is achieved, since 0° and 30° angles of incidence are the

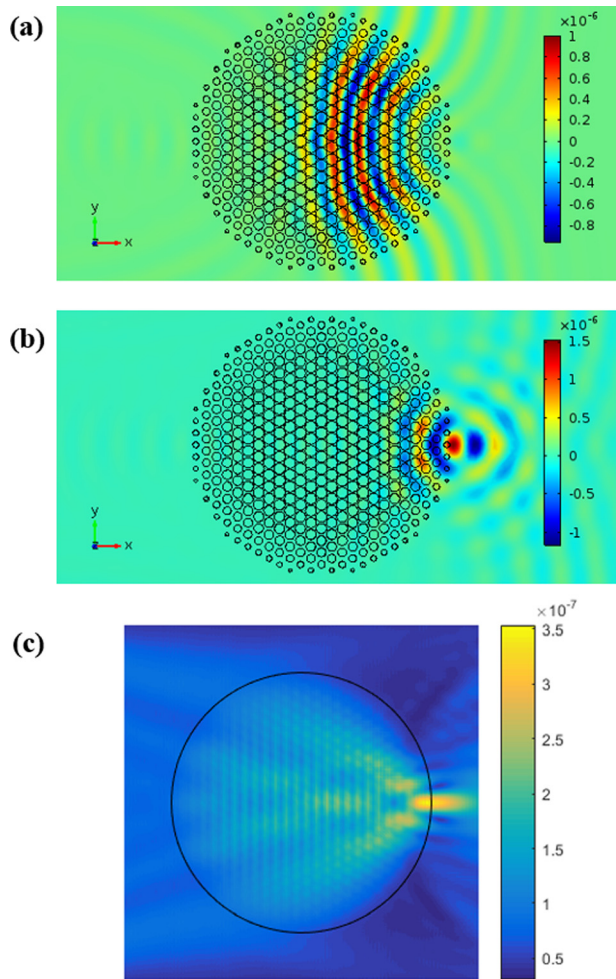


FIG. 2. Numerical simulations for plane wave excitation with 0° angle of incidence: Instantaneous wave fields at (a) $168 \mu\text{s}$ and (b) $212 \mu\text{s}$; and (c) RMS wave field (all results are out-of-plane velocity field in m/s).

two extreme cases according to the unit cell and lens schematics in Fig. 1.

Figure 4 shows the fabricated PC Luneburg lens plate and the experimental setup. Plane wave-like wave fronts were generated at 0° and 30° relative to the x -axis in Fig. 1(f) by two line arrays of piezoelectric disc transducers (5 mm in diameter and 0.4 mm in thickness from STEMiNC Corp.) bonded to the aluminum plate with 10 mm spacing. These transducers were excited by 4 cycles of sinusoidal burst at 50 kHz using a function generator (Agilent 33220A) and a voltage amplifier (Trek Model PZD350). A Polytec PSV-400 scanning laser Doppler vibrometer (LDV) was used to measure the resulting wave field by recording the out-of-plane component of the velocity of the plate over a grid of points covering the lens domain (scanning was performed on the flat side of the plate). With proper triggering of the laser measurements, the wave field was reconstructed. A close-up view of the PC Luneburg lens is given in Fig. 4(b). The scanned side of the plate shown in Fig. 4(c) displays the locations of the harvesters (to be discussed later on).

Figures 5(a) and 5(b) show the measured RMS distribution of the out-of-plane velocity fields for 0° and 30° angles of incidence, respectively, and reveal excellent agreement with the numerical elastic wave simulations at the design frequency, while also validating the omnidirectional aspect of

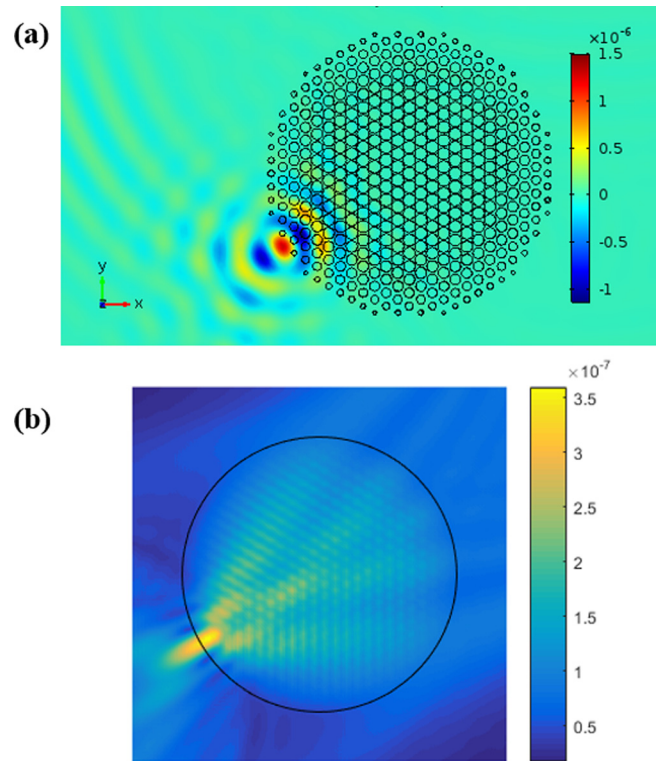


FIG. 3. Numerical simulations for plane wave excitation with 30° angle of incidence: (a) Instantaneous wave field at $212 \mu\text{s}$ and (b) RMS wave field.

focusing using the designed PC Luneburg lens. The incident plane wave focuses at the opposite border with a very similar pattern for both angles of incidence.

Having validated the fabricated PC Luneburg lens design and its omnidirectional focusing performance experimentally, energy harvesting performance enhancement

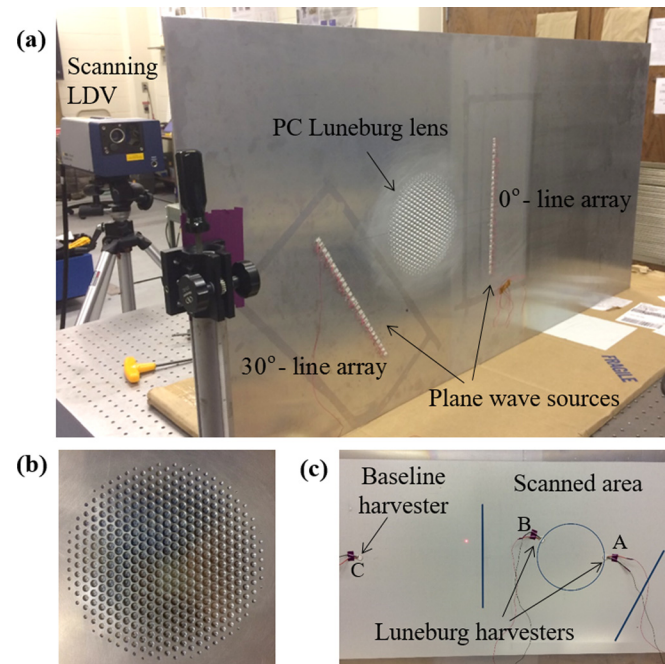


FIG. 4. Experimental setup showing the PC Luneburg lens and the harvester configurations: (a) Overall setup showing the locations and orientations of the line arrays used for plane wave generation; (b) close-up view of the PC Luneburg lens; and (c) locations of the Luneburg harvesters [(A) and (B)] and the baseline harvester (C) on the scanned side of the plate.

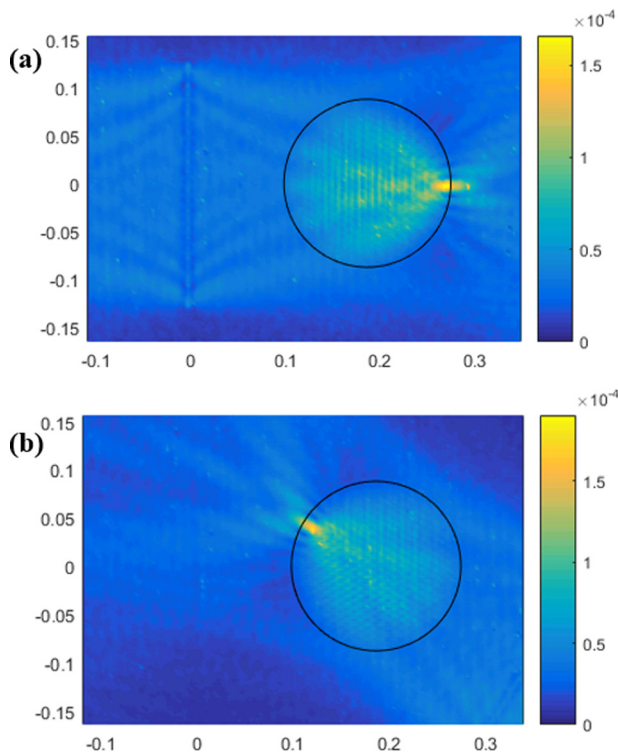


FIG. 5. Experimental RMS wave fields demonstrating omnidirectional focusing performance for (a) 0° and (b) 30° angles of incidence.

associated with this lens is explored next. Identical half-wavelength piezoelectric energy harvester disks were bonded at the edges of the lens domain (focal regions for 0° and 30° excitation—harvesters A and B, respectively) and also in a baseline setting (harvester C) at the same distance from the line array excitation source in the uniform plate region by means of a vacuum bonding technique [on the flat side of the plate shown in Fig. 4(c)]. Energy harvesting experiments were performed with resistor sweep tests by connecting the bottom and top electrodes of the piezoelectric harvesters to a range of resistive electrical loads ($500\ \Omega$ – $2\ \text{k}\Omega$) covering the optimal resistive loading conditions of both the Luneburg-enhanced harvester (A) and the baseline harvester (C) simultaneously under plane wave excitation by the 0° line array [Fig. 4(a)]. Average power outputs of the harvesters were calculated from the voltage measurements across the resistor with an oscilloscope (Tektronix TDS2024). Similarly, the voltage output of other Luneburg-enhanced harvester (B) is measured under the plane wave excitation by the 30° line array. Figure 6(a) shows the measured voltage output signals under the optimal resistive loading of $1.2\ \text{k}\Omega$, and Fig. 6(b) displays the average electrical power with changing load resistance (covering the optimal load). Under the same excitation applied to both harvesters, the harvested power (hence the efficiency) is increased by around 13 times via focusing the elastic waves in the PC Luneburg lens as compared to the baseline case of harvesting incident plane waves using the same piezoelectric disk as the harvester. Hence, the PC Luneburg lens concept integrated with piezoelectric energy harvester yields dramatically enhanced structure-borne elastic wave energy harvesting. As expected, the 30° -incident harvester [i.e., harvester B in Fig. 4(c)] yields similar power levels as the 0° -incident harvester [i.e., harvester A in

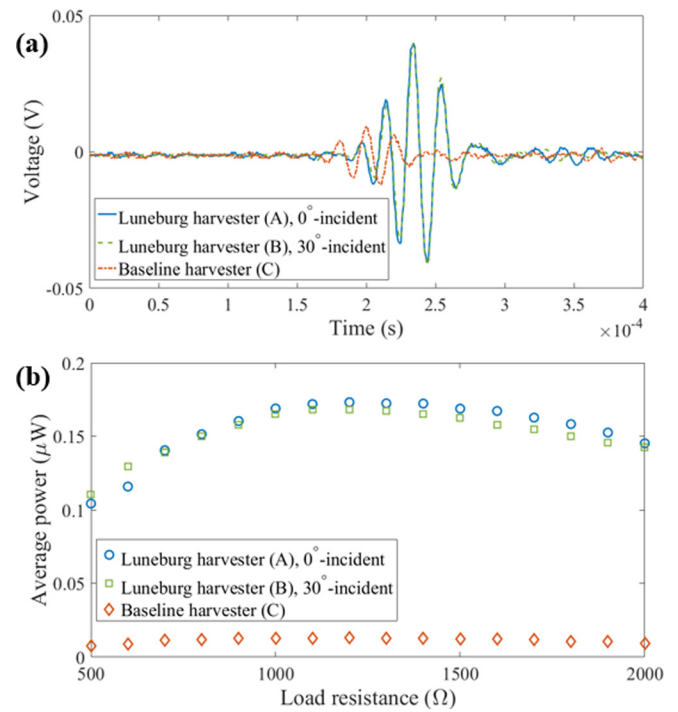


FIG. 6. Energy harvesting performance results of the PC Luneburg lens-based harvesters (for 0° and 30° incident plane waves, i.e., harvesters A and B) and the baseline harvester (i.e., harvester C): (a) Instantaneous voltage histories and (b) average electrical power versus load resistance.

Fig. 4(c)] according to Fig. 6(b). Hence, the omnidirectional plane wave energy harvesting concept is also validated experimentally.

In summary, we presented a phononic crystal-based Luneburg lens employing an axisymmetric gradient index distribution, enabling dramatic performance enhancement by omnidirectional plane wave focusing. We designed, fabricated, and both numerically and experimentally validated a PC Luneburg lens-based elastic wave energy harvester that is composed of blind holes in hexagonal unit cells with varying diameters combined with a piezoelectric disk located at the edge of the lens. The omnidirectionality of the PC Luneburg lens was tested and validated under the excitation of two plane wave sources with 0° and 30° angles of incidence. The harvested power output was enhanced by more than an order of magnitude as compared to a baseline harvester in the uniform plate domain. The omnidirectional focusing capability of the PC Luneburg lens can potentially alleviate the directional sensitivity of existing focusing concepts for enhanced elastic wave energy harvesting by locating multiple energy harvesters along the border of the PC lens domain with separately processed and rectified outputs. Near future efforts include low-frequency lens design and implementation via locally resonant³² unit cells formerly employed in bandgap formation³³ for wave guiding³⁴ and vibration attenuation.^{35,36}

This work was supported in part by the National Science Foundation under Grant No. CMMI-1333978, which is gratefully acknowledged. The authors would also like to thank Dr. Massimo Ruzzene for making the scanning LDV system available.

- ¹P. A. Deymier, *Acoustic Metamaterials and Phononic Crystals*. (Springer-Verlag, Berlin, 2013).
- ²V. Laude, *Phononic Crystals* (Walter de Gruyter GmbH, Berlin, 2015).
- ³M. Sigalas and E. N. Economou, *J. Sound Vib.* **158**, 377 (1992).
- ⁴M. S. Kushwaha, P. Halevi, L. Dobrzynski, and B. Djafari-Rouhani, *Phys. Rev. Lett.* **71**(13), 2022 (1993).
- ⁵J. H. Page, P. Sheng, H. P. Schriemer, I. Jones, X. Jing, and D. A. Weitz, *Science* **271**, 634 (1996).
- ⁶R. Martínez-Sala, J. Sancho, J. V. Sanchez, V. Gomez, J. Llinares, and F. Meseguer, *Nature* **378**, 241 (1995).
- ⁷J. V. Sánchez-Pérez, D. Caballero, R. Martínez-Sala, C. Rubio, J. Sánchez-Dehesa, F. Meseguer, J. Llinares, and F. Gálvez, *Phys. Rev. Lett.* **80**, 5325 (1998).
- ⁸C. J. Rupp, M. L. Dunn, and K. Maute, *Appl. Phys. Lett.* **96**, 111902 (2010).
- ⁹A. Sukhovich, B. Merheb, K. Muralidharan, J. O. Vasseur, Y. Pennec, P. A. Deymier, and J. H. Page, *Phys. Rev. Lett.* **102**, 154301 (2009).
- ¹⁰J. Zhu, J. Christensen, J. Jung, L. Martin-Moreno, X. Yin, L. Fok, X. Zhang, and F. J. Garcia-Vidal, *Nat. Phys.* **7**, 52–55 (2011).
- ¹¹S. C. S. Lin, T. J. Huang, J. H. Sun, and T. T. Wu, *Phys. Rev. B* **79**, 094302 (2009).
- ¹²T. T. Wu, Y. T. Chen, J. H. Sun, S. C. S. Lin, and T. J. Huang, *Appl. Phys. Lett.* **98**, 171911 (2011).
- ¹³A. Climente, D. Torrent, and J. Sánchez-Dehesa, *Appl. Phys. Lett.* **97**, 104103 (2010).
- ¹⁴S. Gonella, A. C. To, and W. K. Liu, *J. Mech. Phys. Solids* **57**(3), 621–633 (2009).
- ¹⁵Z. S. Chen, Y. M. Yang, Z. M. Lu, and Y. T. Luo, *Phys. B: Condens. Matter* **410**, 5–12 (2013).
- ¹⁶K. Mikoshiba, J. M. Manimala, and C. Sun, *J. Intell. Mater. Syst. Struct.* **24**(2), 168–179 (2013).
- ¹⁷L. Zhao, S. C. Conlon, and F. Semperlotti, *Smart Mater. Struct.* **23**(6), 065021 (2014).
- ¹⁸K. H. Sun, J. E. Kim, J. Kim, and K. Song, *Smart Mater. Struct.* **26**, 075011 (2017).
- ¹⁹L. Y. Wu, L. W. Chen, and C. M. Liu, *Appl. Phys. Lett.* **95**, 013506 (2009).
- ²⁰W. C. Wang, L. Y. Wu, L. W. Chen, and C. M. Liu, *Smart Mater. Struct.* **19**, 045016 (2010).
- ²¹H. Lv, X. Tian, M. Y. Wang, and D. Li, *Appl. Phys. Lett.* **102**, 034103 (2013).
- ²²S. Qi, M. Oudich, Y. Li, and B. Assouar, *Appl. Phys. Lett.* **108**(26), 263501 (2016).
- ²³M. Carrara, M. R. Cacan, J. Toussaint, M. J. Leamy, M. Ruzzene, and A. Erturk, *Smart Mater. Struct.* **22**(6), 065004 (2013).
- ²⁴M. Carrara, M. Cacan, M. Leamy, M. Ruzzene, and A. Erturk, *Appl. Phys. Lett.* **100**(20), 204105 (2012).
- ²⁵S. Tol, F. T. Vora, F. L. Degertekin, and A. Erturk, paper presented at the 2016 IEEE sensors (2016).
- ²⁶S. Tol, F. L. Degertekin, and A. Erturk, *Appl. Phys. Lett.* **109**, 063902 (2016).
- ²⁷A. Climente, D. Torrent, and J. Sanchez-Dehesa, *Appl. Phys. Lett.* **105**, 064101 (2014).
- ²⁸Y. Jin, D. Torrent, Y. Pennec, Y. Pan, and B. Djafari-Rouhani, *J. Appl. Phys.* **117**, 244904 (2015).
- ²⁹X. Yan, R. Zhu, G. Huang, and F. G. Yuan, *Appl. Phys. Lett.* **103**(12), 121901 (2013).
- ³⁰J. Zhao, R. Marchal, B. Bonello, and O. Boyko, *Appl. Phys. Lett.* **101**(26), 261905 (2012).
- ³¹T. T. Wu, M. J. Chiou, Y. C. Lin, and T. Ono, *Proc. SPIE* **8994**, 89940G (2014).
- ³²Z. Liu, X. Zhang, Y. Mao, Y. Zhu, Z. Yang, C. T. Chan, and P. Sheng, *Science* **289**(5485), 1734–1736 (2000).
- ³³M. Oudich, Y. Li, B. M. Assouar, and Z. Hou, *New J. Phys.* **12**(8), 083049 (2010).
- ³⁴M. Oudich, M. B. Assouar, and Z. Hou, *Appl. Phys. Lett.* **97**(19), 193503 (2010).
- ³⁵C. Sugino, S. Leadenham, M. Ruzzene, and A. Erturk, *J. Appl. Phys.* **120**(13), 134501 (2016).
- ³⁶C. Sugino, Y. Xia, S. Leadenham, M. Ruzzene, and A. Erturk, *J. Sound Vib.* **406**, 104–123 (2017).